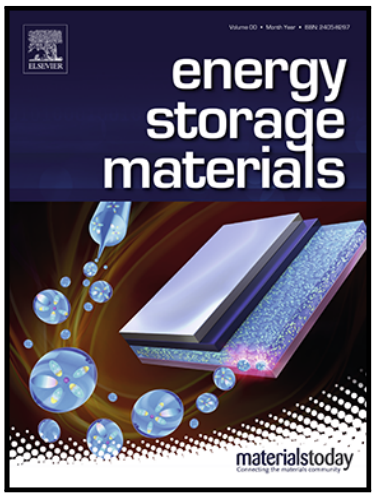

Ultrafast Lattice Engineering for High Energy Density and High-Rate Sodium-Ion Layered Oxide Cathodes

Bizhu Zheng , Hui Qian , Gangya Cheng , Chen Yuan , Yong Cheng , Ming-Sheng Wang , Xiangsi Liu , Yuxuan Xiang

PII: S2405-8297(24)00694-9
DOI: https://doi.org/10.1016/j.ensm.2024.103868
Reference: ENSM 103868

To appear in: *Energy Storage Materials*

Received date: 10 August 2024
Revised date: 20 October 2024
Accepted date: 25 October 2024

Please cite this article as: Bizhu Zheng , Hui Qian , Gangya Cheng , Chen Yuan , Yong Cheng , Ming-Sheng Wang , Xiangsi Liu , Yuxuan Xiang , Ultrafast Lattice Engineering for High Energy Density and High-Rate Sodium-Ion Layered Oxide Cathodes, *Energy Storage Materials* (2024), doi: https://doi.org/10.1016/j.ensm.2024.103868

Ultrafast Lattice Engineering for High Energy Density and High-Rate Sodium-Ion Layered Oxide Cathodes

Bizhu Zheng[a,b,c,†], Hui Qian[a,b,c,†], Gangya Cheng[a,b,c], Chen Yuan[a,b,c], Yong Cheng[d], Ming-Sheng Wang[d], Xiangsi Liu[a,b,c,*], Yuxuan Xiang[a,b,c,*]

[a] *Research Center for Industries of the Future, Westlake University, Hangzhou 310030, Zhejiang, China*

[b] *School of Engineering, Westlake University, Hangzhou 310030, Zhejiang, China*

[c] *Institute of Advanced Technology, Westlake Institute for Advanced Study, Hangzhou 310024, Zhejiang, China*

[d] *State Key Laboratory for Physical Chemistry of Solid Surface, College of Materials, Xiamen* ***University, Xiamen 361005, China***

Keywords: Sodium-ion layered oxides, Non-equilibrium synthesis, Manganese-ion vacancies, Crystal structure evolutions, Local environment

The authors marked with a dagger (Bizhu Zheng, Hui Qian) are designated as co-first authors. The asterisk symbol (Xiangsi Liu, Yuxuan Xiang) indicates co-corresponding authors.

For your reference, the corresponding authors' details are as follows:

Xiangsi Liu: liuxiangsi@westlake.edu.cn
Yuxuan Xiang: xiangyuxuan@westlake.edu.cn

Abstract:

Sodium-ion batteries attract significant interest for large-scale energy storage owing to abundant sodium reserves, while challenges remain in the high synthesis energy consumption, long synthesis period, and poor electrochemical performance of sodium-ion layered oxide materials. This study presents a general high-temperature thermal shock (HTS) strategy to synthesize and optimize sodium-ion layered oxides. The rapid ramping, sintering, and cooling processes minimize volatile sodium loss during HTS, facilitating the improvement of phase purity and effectively optimizing the microstructure of materials in a non-equilibrium state. As a proof of concept, Mn-based $Na_{0.67}MnO_2$ treated with HTS (NMO-HTS) suppresses Mn ion vacancy within transition material layers, thereby increasing the redox centers and lowering the Mn *3d* orbital energy level. Besides, the formation of transition metal layer stacking faults mitigates the structural transformation and Na^+-vacancies ordering arrangement during cycling. Consequently, the energy density of the NMO-HTS increases by 21.5% to 559 Wh kg^{-1}, with an outstanding rate capability of 108 mAh g^{-1} at 10C and an impressive capacity retention of 93.7% after 300 cycles at 1C. In addition, we demonstrate the universality of HTS in synthesizing various other sodium-ion layered oxides, including nickel-based and iron-based cathodes, as well as in activating degraded materials.

1. Introduction

Driven by the imperative to address challenges arising from the limited natural abundance and uneven global distribution of lithium resources, both academia and industry have directed efforts toward exploring cost-effective electrochemical energy storage technologies [1,2]. Sodium-ion batteries (SIBs), akin to lithium-ion batteries but benefiting from a broader range of raw material sources, stand out in the next-generation energy storage technologies with considerable commercial potential [3,4]. Nevertheless, the practical advantages of SIBs have not been conclusively demonstrated due to current limitations in their energy-intensive and time-consuming material synthesis processes, inadequate manufacturing supply chains, and inferior cycle performance [4,5]. To promote the widespread commercial adoption of SIBs, a critical emphasis should be placed on their low-cost characteristics.

Given that cathode materials constitute a significant portion of the full battery cost, exceeding 30%, and represent pivotal components influencing the overall electrochemical performance of SIBs, there exists an imperative need to reduce material expenses while concurrently improving cathode electrochemical performance [6]. Among various cathode materials, sodium-ion layered oxides, characterized by a periodic alternating arrangement of transition metal (TM) layers and sodium layers along the crystallographic z-axis, have attracted considerable attention [7]. Particularly, layered oxides with P2 and O3 structures have demonstrated preliminary commercial applications, owing to their facile one-step sintering synthesis and notable practicality [8-11]. Compared to O3-type materials, P2-type materials exhibit fewer phase transitions during cycling, larger interlayer spacing, and faster Na^+ transport

within the two-dimensional channel, thereby enabling superior cycling stability and rate performance[12-14].

The synthesis processes profoundly impact the crystalline structure and the ion transport mechanism of materials, consequently influencing the electrochemical performance of electrodes [15-17]. In the case of cost-effective P2/P2'-type $Na_{0.67}MnO_2$ (NMO), high-temperature calcination followed by natural cooling induces an oxygen absorption reaction, as revealed by TGA analysis[18], leading to the formation of Mn vacancies (MVs) within the TM layers. The formation of MVs has been confirmed by EPR[19], X-ray diffraction[20], neutron diffraction[20,21], and aberration-corrected electron microscopy[22]. Moreover, magnetic testing and chemical titration further verified that the formation of MVs results in an increase in the average valence state of Mn ions, leading to the formation of the P2 phase (space group: $P6_3/mmc$)[23]. Conversely, fast-cooling treatments would minimize MVs and increase Mn^{3+} content, inducing a prominent cooperative Jahn-Teller effect in the crystal lattice, ultimately forming the distorted P2' phase (space group: *Cmcm*) [18-20,24]. Beyond modulating the crystalline structure, the synthesis processes play a pivotal role in regulating the ion transport mechanisms of NMO during cycling. Prolonged solid-state sintering results in the material exhibiting ordered interlayer and intralayer arrangements [25]. Within the Na layers, the ordered arrangement between Na^+ ions and vacancies in different charge states of the electrode is governed by the intricate interplay between TM ion distributions and electrostatic forces, which would elevate the energy barrier for Na^+ transport [26]. Accordingly, disrupting the ordered interlayer spacing or introducing heterovalent metal ions into the crystal lattice can hinder the ionic ordering arrangement within the Na and TM layers, which impedes the Na^+-

vacancy ordering phenomenon and enhances Na^+ mobility during the electrochemical process [27-30].

However, the synthesis of P2-type layered oxides through conventional solid-state reaction and sol-gel methods typically requires high-temperature calcination lasting several tens of hours, demanding a substantial investment in energy and time[10,31,32]. Moreover, this prolonged calcination period inevitably leads to the loss of volatile components, such as sodium salts, not conducive to the synthesis of pure phase structures. Additionally, introducing advantageous structural defects into electrode materials has been extensively utilized to enhance the performance of energy materials [15,33-35]. Facilitating the formation of structural defects requires rapid quenching from high temperatures or other non-equilibrium conditions [20,27,34,36]. However, limited by slow heating and cooling rates and constrained reaction kinetics, conventional synthesis methods are hard to ensure the uniform distribution of dopants and the precise regulation of the phase and defect composition [37,38]. Consequently, the prepared cathodes usually show a capacity limited to below ~180 mAh g^{-1} based on TM redox reactions [39]. In short, the high energy consumption and lengthy period during material synthesis processes, as well as lower-than-expected electrochemical performance, still fail to meet the cost demands of SIBs for large-scale energy storage applications.

In this work, for the first time, the high-temperature shock (HTS) technique is utilized for the ultrafast synthesis of sodium-ion layered oxide materials. Through sintering by Joule-heated strips, HTS achieves rapid ramping (~ 10^4 °C min^{-1}) and cooling rates (~10^3 to 10^4 °C min^{-1}), thus enabling a substantial reduction in material sintering energy and time while tuning the crystal structure and properties of the material in a non-equilibrium state [15,38,40-43]. By

employing cost-effective Mn-based P2-$Na_{0.67}MnO_2$ (NMO) as a representative material, we have investigated the effects of the HTS method versus the conventional solid-state method on the crystal structural, local environmental, morphological, and performance correlations in sodium-ion layered oxides. As illustrated in **Fig. 1a**, HTS enables the ultra-rapid synthesis of NMO materials within tens of seconds, while eliminating MVs in TM layers, leading to a higher practical discharge capacity and operational voltage. Besides, the non-equilibrium synthesis conditions induced by HTS result in the formation of TM layer stacking faults in NMO. This effectively mitigates the vexing interlayer Na-vacancy ordering and multiple structural phase transformations during charge-discharge cycling, endowing the cathode with remarkable rate capability and cycling stability. Beyond Mn-based materials, the HTS technique has been demonstrated to be successfully applicable to a variety of sodium-ion layered oxide materials, including Fe-based, Ni-based, degraded materials, and even facilitates the pure-phase synthesis of multiple heterovalent element-doped materials, which are unattainable through conventional synthesis methods. The presented high-efficiency and universally applicable synthesis methodology catalyzes the integration of sodium-ion layered oxide cathodes into the development of advanced SIBs.

2. Experimental Section

2.1 Materials synthesis: A series of $Na_xM_yMn_{1-y}O_2$ ($0 \leq y$, M = Li^+, Mg^{2+}, Ni^{2+}, Al^{3+}, Fe^{3+}, and Ti^{4+}) materials were prepared using a sol-gel method followed by different high-temperature sintering processes. According to the stoichiometric ratio of the target material, CH_3COONa (3 wt.% excess, ≥99.0%), $Mn(CH_3COO)_2 \cdot 4H_2O$ (≥99.0%), CH_3COOLi (3 wt.% excess, ≥99.0%),

$Mg(CH_3COO)_2•4H_2O$ (≥99.0%), $Ni(CH_3COO)_2•4H_2O$ (≥99.0%), $Al(NO_3)_3•9H_2O$ (≥99.0%), $Fe(NO_3)_3•9H_2O$ (≥99.0%), and $Ti(C_2O_4)_2$ (≥99.0%), were dissolved in 50 mL of distilled water. The citric acid ($Na_xM_yMn_{1-y}O_2$: $C_6H_8O_7$ = 2 : 1 in mole ratio) was added to the resulting solution, with $NH_3•H_2O$ (28%) used to adjust the pH to 7-8. The mixture was heated to 80°C and stirred for 12 h to form a sol. Subsequent drying at 120°C for 12 h yielded a gel. Then, the mixture was calcined at 450°C for 6 h to produce the desired precursor material. For the muffle furnace-sintered (MF) samples, the precursor powder underwent re-grinding and compaction into pellets. These pellets were then subjected to calcination at 900°C for a duration of 15 hours under an oxidizing atmosphere, followed by rapid quenching to ambient temperature and subsequent storage within an argon-filled glove box. For the NMO-MF-SC sample, it was quenched after high-temperature sintering with a cooling rate of 2°C min^{-1} down to 500°C. In the case of the high-temperature shock (HTS) samples, the HTS treatment was executed through electric joule heating in an ambient air setting. The precursor powder underwent re-grinding and was positioned atop a 1 mm-thick nickel substrate. The sample temperature was elevated to predetermined set points within approximately 10 s and maintained for 60 s. Temperature modulation was accomplished utilizing an infrared detector and the samples were finally stored in an argon-filled glove box.

2.2 Electrochemical measurements: The cathode was fabricated by applying a slurry composed of active materials, acetylene black, and polyvinylidene fluoride (in a weight ratio of 8:1:1) onto an aluminum foil substrate. N-methyl-2-pyrrolidone served as the solvent for the slurry. The coated substrates were subsequently dried under vacuum conditions at 120°C overnight. Sodium metal was employed as the anode, and a 1 M $NaClO_4$ in PC solution

containing 5% FEC or NaFSI : DME : BTFE = 1 : 2 : 4 in mole ratio was used as the electrolyte. The assembled cells were encapsulated within 2016-type coin cell housings. The electrochemical performance of the cells was evaluated using a Neware CT-4008 battery testing system, where the cells underwent galvanostatic charge-discharge cycles. For the galvanostatic intermittent titration technique (GITT) analyses, cycling was performed at a current density of 24 mA g^{-1}, and the duration time for each applied galvanostatic current and rest was 5 and 50 min, respectively. Temperature-dependent electrochemical tests were conducted using a Neware MGDW-225-40-5V20mA160CH battery testing system. For full-cell assembly, the synthesized NMO-HTS material was used as the cathode with a mass loading of 4.0 mg cm^{-2}, while hard carbon (Canrd New Energy Technology Co., Ltd.) served as the anode with a mass loading of 3.13 mg cm^{-2}. The electrolyte consisted of 1.0 mol L^{-1} $NaClO_4$ dissolved in a mixed solvent of ethylene carbonate (EC) and diethyl carbonate (DEC) in a 50:50 volume ratio. To presodiate the cathode and compensate for the irreversible capacity of hard carbon during the first cycle, the NMO-HTS electrode was first assembled with sodium metal to form a half-cell, followed by a 10 s short-circuit by connecting the cathode and Na anode with a metal wire. A separate half-cell was assembled with the hard carbon anode and sodium metal, and subjected to a single-cycle of sodium pre-intercalation and deintercalation between 0.005 and 2.5 V at 24 mA g^{-1}.

2.3 Material characterizations: The particle size distribution of the powder materials was determined using a Laser Diffraction Particle Size Analyzer (Malvern, MASTERSIZER 3000). The elemental stoichiometry of each sample was determined using Optima 2000-DV inductively coupled plasma emission spectrometry (ICP-OES, PerkinElmer). X-ray diffraction

(XRD) patterns were acquired using a Bruker D8 Advance diffractometer equipped with Cu Kα radiation (λ=1.5406 Å), covering a 2θ range of 10-80 degrees. The obtained XRD data underwent Rietveld refinement analysis utilizing the General Structure Analysis System (GSAS) software [44]. Scanning electron microscopy (SEM, Phenom Pharos G2) was employed for morphological characterization, complemented by energy-dispersive X-ray spectroscopy (EDS) for elemental analysis at an operating voltage of 15 kV. High-resolution transmission electron microscopy (HRTEM) images were obtained using a FEI Talos F200S operated at 200 keV. Solid-state nuclear magnetic resonance (SS NMR) spectra were recorded on a 500 MHz Solid-State NMR Spectrometer with a BRUKER 1.3 mm triple resonance (H/X/Y) 500 MHz CP-MAS WB DVT probe spinning at 55 kHz. For the ^{23}Na NMR experiments, parameters were set to a recycle delay of 0.02 s and a 90° pulse length of 1.6 μs for the spin-echo pulse. A projection-magic angle turning phase-alternating spinning sideband (pjMATPASS) pulse sequence was employed to acquire isotropic ^{23}Na NMR spectra. X-ray photoemission spectroscopy (XPS) was performed using an ESCALAB Xi+ spectrometer, while electron paramagnetic resonance (EPR) experiments were conducted on a Bruker EMXplus-6/1 instrument. The water content within the samples was determined through thermal gravimetric analyzer (TGA) using a Spectrum3-Spotlight400-Clarus SQ8 GC/MS system. The volumetric capacity (Cv) of the material was calculated using the following formula. The compact density (ρ) was determined by pressing ~1g of powder material into a 10 mm diameter pellet under a pressure of 10 MPa, followed by measuring the pellet's thickness for compact density calculation.

$$Cv = \frac{m \times Cg}{V} = Cg \times \rho$$

2.4 DFT calculation details: First-principles calculations were conducted using Density Functional Theory (DFT) implemented in the Vienna Ab initio Simulation Package (VASP) to assess the density of states (DOS) for samples with varying Mn vacancy concentrations [45]. The Perdew–Burke–Ernzerhof (PBE) exchange-correlation functional and projector-augmented wave (PAW) methods were employed for optimization [46,47]. To ensure calculation accuracy, an energy cut-off of 550 eV and a 4 × 4 × 3 k-point grid were utilized. Convergence criteria for forces and energies were set to 0.01/Å and 10^{-6} eV, respectively. The GGA+U method, with Hubbard U terms of 3.9 eV for Mn 3d bands, was employed to obtain precise DOS results.

3. Results and Discussion

3.1 Synthesis and Characterization of NMO Materials

The synthesis of NMO materials was conducted by employing conventional solid-state reactions and HTS strategies on precursors. Varying synthesis temperatures from 600 °C to 1000 °C (**Fig. S1**), X-ray diffraction (XRD) patterns show desired crystal structure is obtained at 1000 °C. Owing to the exceptionally fast ramping and cooling rate, HTS reaches the targeted temperature within 10 s and the whole HTS sintering process can be achieved within 70 s compared to 18 h by muffle furnace (MF) sintering **(Fig. 1b)**. Meanwhile, this ultrafast HTS sintering process effectively reduces the volatilization of Na salts and improves the crystalline phase purity of NMO-HTS. As indicated by ICP-OES analysis (**Table S1**), the sodium content in NMO-HTS is higher than that in NMO-MF. A comparison of the XRD patterns and refined results for NMO-MF and NMO-HTS (**Fig. S2-3 and Table S2**) reveals that NMO-HTS has

pure P2' phase (space group: *Cmcm*) while NMO-MF exists in the form of a mixture of P2' phase and P2 phase (space group: $P6_3/mmc$). This result is consistent with previous research that accelerated material cooling rate is conducive to achieving the pure P2' phase [20,23]. Moreover, the intensity of the diffraction peak in NMO-HTS is lower than that of NMO-MF, which may be attributed to the smaller particle size of NMO-HTS as shown in SEM images (**Fig. 1e-f**) and lower crystallinity under such metastable synthesis conditions provided by the HTS. The reduced particle size in NMO-HTS means an increase in its specific surface area, which is expected to improve contact with the electrolyte, enhance material utilization, and shorten the ion transport distance. In short, the HTS strategy enables the ultrafast synthesis of NMO materials in ~70 s, and this rapid sintering and annealing process significantly regulates the crystal structure and microscopic morphology of materials into a pure long-range crystal structure and small particle size.

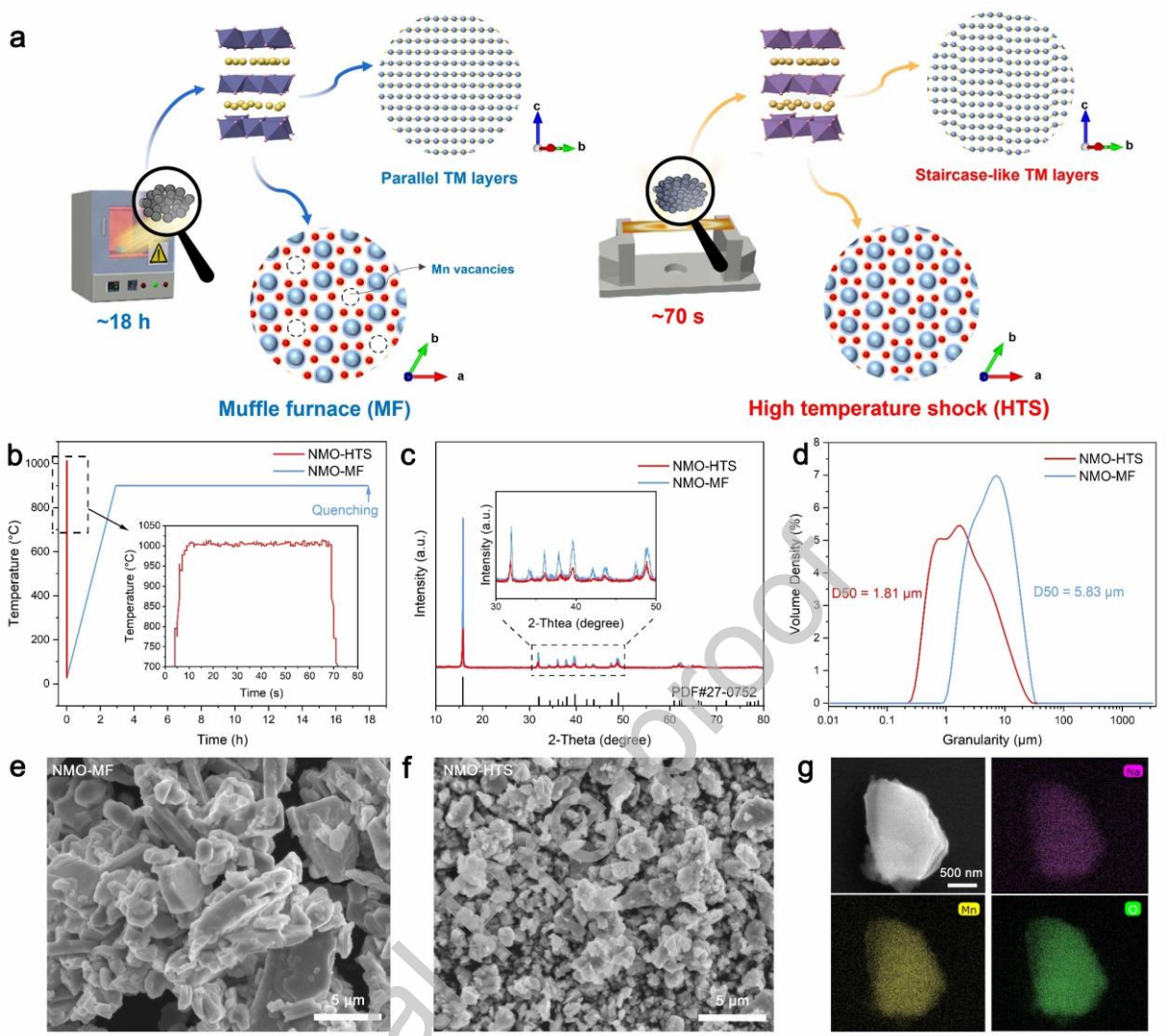

Fig. 1. Synthesis and characterization of NMO materials. a) Schematic diagram of the synthesis process and the atom-scale structure for NMO materials by employing a muffle furnace sintering and high-temperature shock technique. b) Temperature curves during conventional muffle furnace sintering and HTS processes, with an inset showing an enlarged view of the temperature profile of the HTS process. c) XRD patterns of NMO-HTS and NMO-MF materials, with an inset showing an enlarged view of the 30°-50° range. d) Particle size measurements for NMO-HTS and NMO-MF materials. SEM images of e) NMO-MF and f) NMO-HTS, along with g) EDS images of NMO-HTS.

3.2 Microstructural Differences Between NMO-MF and NMO-HTS

High-resolution transmission electron microscopy (HRTEM) was employed to characterize the microstructural difference between NMO-MF and NMO-HTS, as shown in **Fig. 2a-b**. In the HRTEM images, local magnification reveals that the lattice spacings of NMO-MF and NMO-

HTS are 0.53 and 0.56 nm, respectively, consistent with the interlayer spacing of the (002) plane. It is noteworthy that, in contrast to the regular stacking sequence and continuous extension of TM layers observed in the NMO-MF, the TM layers in NMO-HTS exhibit stacking fault distribution where TM layers are misaligned. Specifically, after a certain length of smooth continuation, the TM layers in NMO-HTS undergo a staircase-like transition, leading to the formation of a twisted region at each transition point, which is discernible across various regions at low magnification (**Fig. S4**). Moreover, the (002) peak extracted from the powder XRD spectra (**Fig. S5**) demonstrates that the NMO-HTS exhibits an asymmetric distribution at lower diffraction angles, unlike the symmetrical peak shape observed in NMO-MF. This asymmetry is indicative of the heterogeneous distribution of TM layer stacking faults in the long-range structure of NMO-HTS. We speculate that the formation of the TM layer should stem from the short and non-equilibrium synthesis process, preventing the orderly arrangement of the transition metal layers.

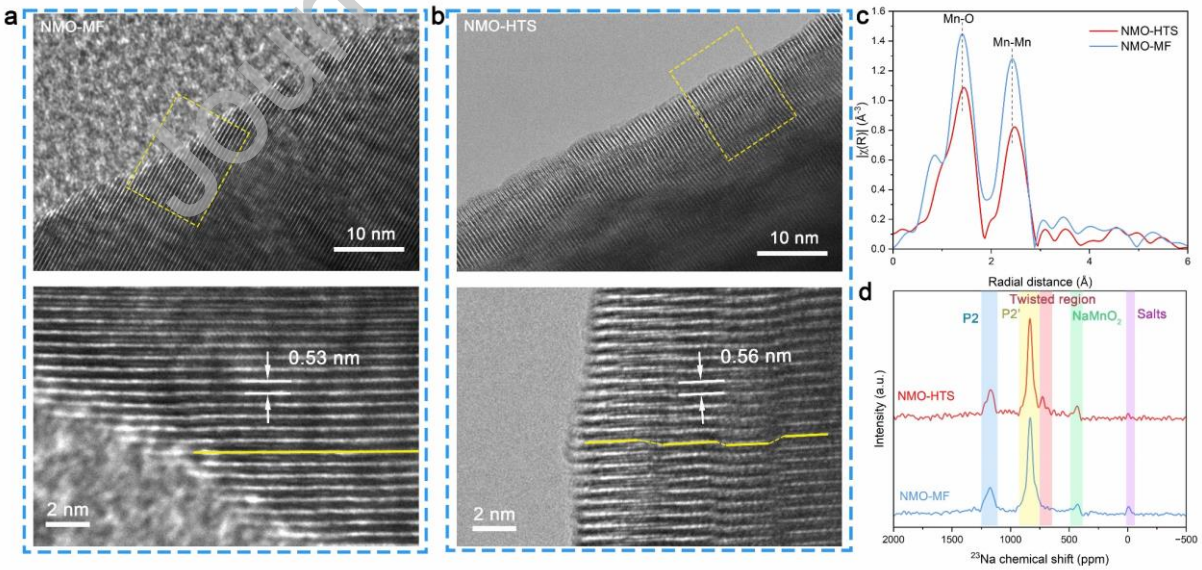

Fig. 2. Characterization of the microstructure. a) HRTEM images of NMO-MF and b) NMO-HTS, with the bottom images showing enlarged views of the areas outlined by yellow dashed

boxes. c) Mn K-edge EXAFS spectra of NMO-MF and NMO-HTS powder samples. d) ^{23}Na SS NMR spectra of NMO-MF and NMO-HTS materials.

To further explore the impact of the TM layer stacking faults on the short-range structure, extended X-ray absorption fine structure (EXAFS) and solid-state nuclear magnetic resonance (SS NMR) techniques were performed to obtain averaged short-range information complementary to TEM results. The comparative results from EXAFS analysis (**Fig. 2c**) indicate that the average Mn-O (first shell) and Mn-Mn (second shell) distances in NMO-HTS are both greater than those in NMO-MF, and their intensities are significantly lower than those in NMO-MF. These observations are consistent with the presence of TM layer stacking faults in NMO-HTS, leading to increased disorder in the interlayer structure [32]. Moreover, as shown in **Fig. 2d**, signals in ^{23}Na NMR spectra corresponding to the P2 and P2' phases occur at ~1170 ppm and ~833 ppm [28,48], respectively, for both NMO-MF and NMO-HTS samples. This contrasts with the above XRD results, where characteristic diffraction peaks of the P2 phase are not detected in NMO-HTS. This disparity should arise from the differing characterization scales of NMR and XRD techniques, *i.e.* NMR reflects the influence of the nearest two TM ion coordination layers around Na^+, while XRD is sensitive to the periodic arrangement of unit cells [28], suggesting that NMO-HTS also contains some local structural characteristics consistent with the P2 phase, even though there is an absence of apparent periodicity in the long-range structure. Additionally, minor signals of O3-type $NaMnO_2$ that cannot be detected in XRD and antiferromagnetic sodium salts are detected at ~435 ppm and ~0 ppm respectively for both NMO-MF and NMO-HTS [49]. Most importantly, an obvious peak appears at ~723 ppm in the ^{23}Na NMR spectrum of NMO-HTS. We attribute this peak to Na^+ situated within the twisted

region of TM layer stacking faults, where the anisotropic bulk atomic susceptibility (χ) and the low local symmetry contribute to a decreased ^{23}Na chemical shift compared to that of the P2' phase signal [15].

3.3 Electrochemical Properties of NMO-MF and NMO-HTS

Aiming to characterize the electrochemical performance of electrodes in practical application scenarios, the voltage range of galvanostatic charging-discharging experiment was set at 2-4 V to avoid the occurrence of complex anion redox reactions at high voltage [21]. **Fig. 3a-b** illustrates the initial charge-discharge curves of NMO-MF and NMO-HTS cathodes. NMO-HTS demonstrates a high discharge capacity of 211 mAh g^{-1} (754 mAh cm^{-3}) at 24 mA g^{-1}, significantly surpassing that of NMO-MF (184 mAh g^{-1}, 661 mAh cm^{-3}). While the NMO-MF and NMO-HTS electrodes display similar initial charge capacities, primarily due to the reliance of NMO materials on Mn^{3+}/Mn^{4+} redox couples for charge compensation in the low-voltage region (~2.3 V), and the smaller particle size of the NMO-HTS electrode increases the degree of sodium loss during electrode preparation (**Fig. S6**). Moreover, NMO-HTS exhibits a higher average discharge voltage of 2.65 V in comparison to NMO-MF of 2.50 V, resulting in an impressive specific energy density of 559 Wh kg^{-1} (based on the weight of the cathode) for the NMO-HTS cathode, which is comparable to that of state-of-the-art $LiFePO_4$ cathodes, approximately 550 Wh kg^{-1} [50]. Given the initial sodium content of ~0.67, both NMO-MF and NMO-HTS electrodes exhibit a first-cycle charge capacity lower than their discharge capacity. As a result, pre-sodiation is necessary for full cell assembly, as shown in the Experimental Section. When matched with hard carbon in a coin cell (**Fig. S7**), the energy density of the full

cell achieves 248 Wh kg^{-1} (based on the weight of both cathode and anode). Notably, many small plateaus are observed in the charge-discharge curves of NMO-MF, which is distinctly shown in the dQ/dV plot (**Fig. 3c**). While these peak intensities of NMO-HTS at 2.07, 2.22, 2.55, 2.71, and 3.05 V show significant decreases or even disappearances. Besides, several sharp peaks observed around 2.31, 2.92, and 3.52 V in NMO-MF merge into more suppressed peaks in NMO-HTS, corresponding to the alleviated Na^+-vacancy ordering during cycling in NMO-HTS [29,51]. To assess the rate capability and cyclability of the electrodes, the galvanostatic cycling experiments were conducted at different current densities ranging from 240 (1C) to 4800 mA g^{-1} (20C). As shown in **Fig. 3d-e**, NMO-HTS shows significantly higher capacities than NMO-MF at each current density. Specifically, NMO-HTS delivers capacities of 180, 149, 108, and 67 mAh g^{-1} at current densities of 1C, 5C, 10C, and 20C mA g^{-1}, respectively. In contrast, NMO-MF barely shows capacities of 155, 107, 83, and 28 mAh g^{-1} at the corresponding current densities. Note that the application of sodium-ion batteries primarily targets large-scale energy storage devices, thus demanding superior high-/low-temperature performance. As shown in **Fig. 3f and S8**, within the tested temperature range from -25°C to 45°C, the NMO-HTS electrode consistently exhibits a capacity of at least 10 mAh g^{-1} higher than that of the NMO-MF. Particularly, the NMO-HTS electrode surpasses the NMO-MF electrode by 23 mAh g^{-1} and 19 mAh g^{-1} at 45°C and -25°C, respectively. However, negligible improvement can be observed in the cycle stability of NMO-HTS compared to NMO-MF (**Fig. 3d-e**), which should be partly attributed to the smaller particle size of NMO-HTS, exposing larger interfaces and thereby inducing more pronounced interface side reactions.

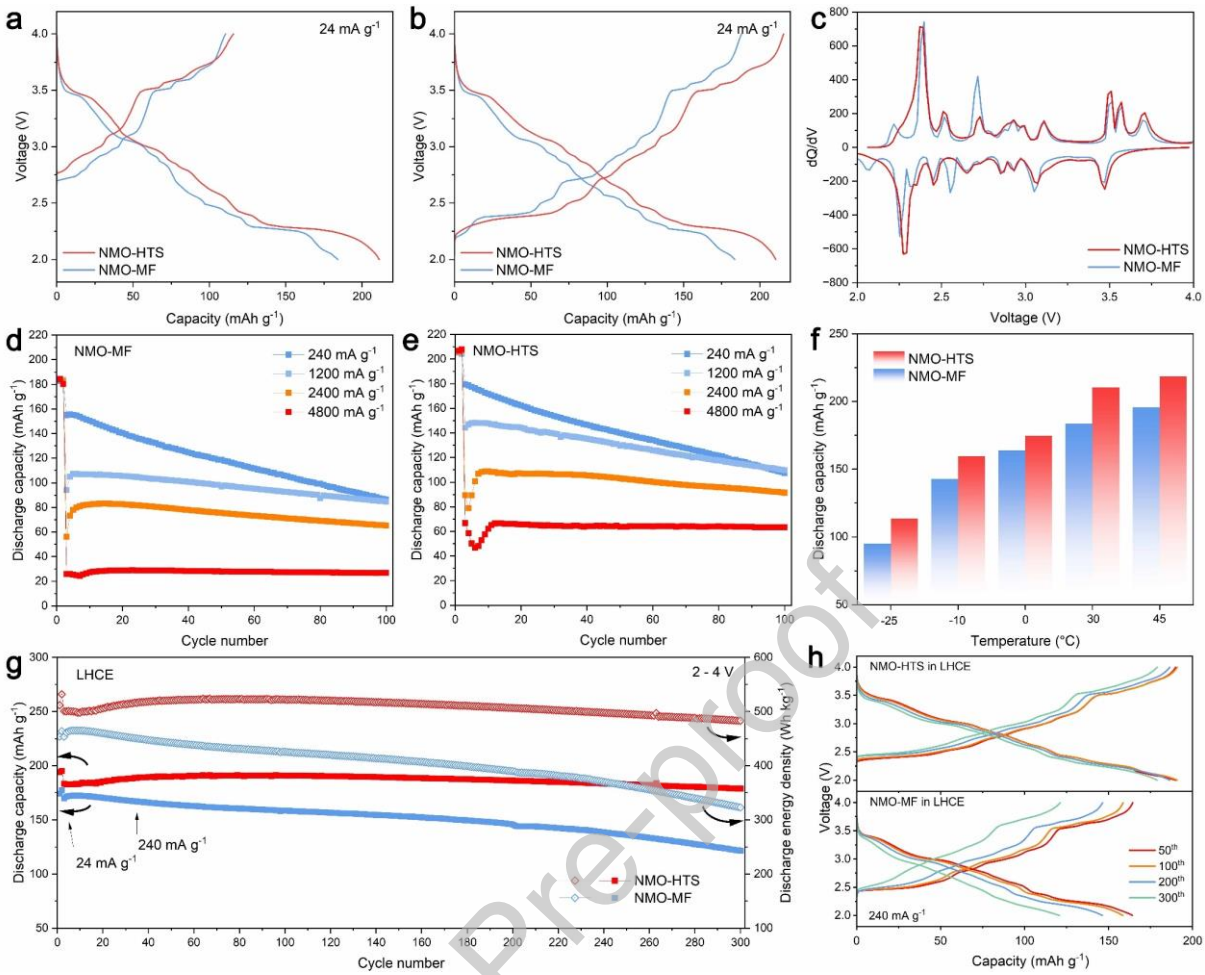

Fig. 3 Electrochemical performance comparison between NMO-MF and NMO-HTS materials. a) The 1st and b) 2nd cycle charge-discharge curves of NMO-MF and NMO-HTS electrodes, along with c) the dQ/dV curves of the 2nd cycle. Cycling performance of d) NMO-MF and e) NMO-HTS electrodes at various current densities ranging from 240 to 4800 mA g^{-1} within the voltage range of 2 - 4 V. f) Discharge capacity of NMO-MF and NMO-HTS electrodes at 24 mA g^{-1} and temperatures ranging from -25°C to 45°C. g) Cycling performance of NMO-MF and NMO-HTS electrodes in LHCE, and h) charge-discharge curves at the 50th, 100th, and 200th cycles.

Herein, to minimize the influence of the interfacial side reactions, we evaluated its extended cycling performance using an LHCE (NaFSI : DME : BTFE = 1 : 2 : 4 in mole ratio) [52,53], and the results are shown in **Fig. 3g-h**. Surprisingly, NMO-HTS shows outstanding electrochemical performance. At the current density of 24 mA g^{-1}, NMO-HTS exhibits a capacity of 198 mAh g^{-1}. Even under a 10-fold increase in current density, it maintains a capacity of 191 mAh g^{-1}, highlighting exceptional rate capabilities. Particularly noteworthy is

the stable cycling performance of the NMO-HTS electrode with LHCE, maintaining a discharge capacity of 179 mAh g^{-1} after 300 cycles, corresponding to a high capacity retention of 93.7% (only 70.7% for NMO-MF). Furthermore, the discharge curve of the 300th cycle closely overlapped with that of the 50th cycle (**Fig. 3h**), indicating negligible voltage decay in the NMO-HTS electrode. The outstanding capacity and voltage retention collectively result in the NMO-HTS electrode delivering an initial energy density of 521 Wh kg^{-1} at 240 mA g^{-1}, which remains at 483 Wh kg^{-1} after 300 cycles with an energy retention of 92.7% (only 69.4% for NMO-MF). The above results confirm that NMO materials synthesized using the HTS technique could suppress the Na^+-vacancy ordering arrangement during electrochemical processes, exhibiting high energy density and outstanding rate capability. Appropriate interface modifications, such as electrolyte adjustment, further offer the potential to achieve long cycling performance.

3.4 The Effects of TM Layers Stacking Faults in NMO-HTS

Disrupting the interlayer spacing of the TM layer or intra-layer ordering of TM ions in NMO materials has been proven to suppress the Na^+-vacancy ordering in Na layers, thereby enhancing Na^+ mobility [27,29]. The galvanostatic intermittent titration (GITT) experiments were conducted to investigate the influence of the TM layer stacking faults on ionic transport in NMO materials. The GITT profiles and the calculated Na^+ diffusion coefficients (D_{Na+}) are presented in **Fig. 4a-b**. It is observed that there are many small plateaus manifest in the GITT curve of NMO-MF, accompanied by obvious voltage polarization, corresponding to the sluggish diffusion of Na^+ in these plateau regions. In contrast, the TM layer stacking faults in NMO-HTS induce increased disorder in the arrangement of TM layers and Na layers, obstructing the

Na^+-vacancy ordering during the cycling. As a result, NMO-HTS exhibits a smooth GITT curve with negligible voltage polarization. Furthermore, as shown in **Fig. 4b,** the calculated geomean value of D_{Na+} for NMO-HTS (3.314×10^{-11} cm^2 s^{-1}) is an order of magnitude higher than that for NMO-MF (3.075×10^{-12} cm^2 s^{-1}), confirming the enhanced Na^+ mobility in NMO-HTS.

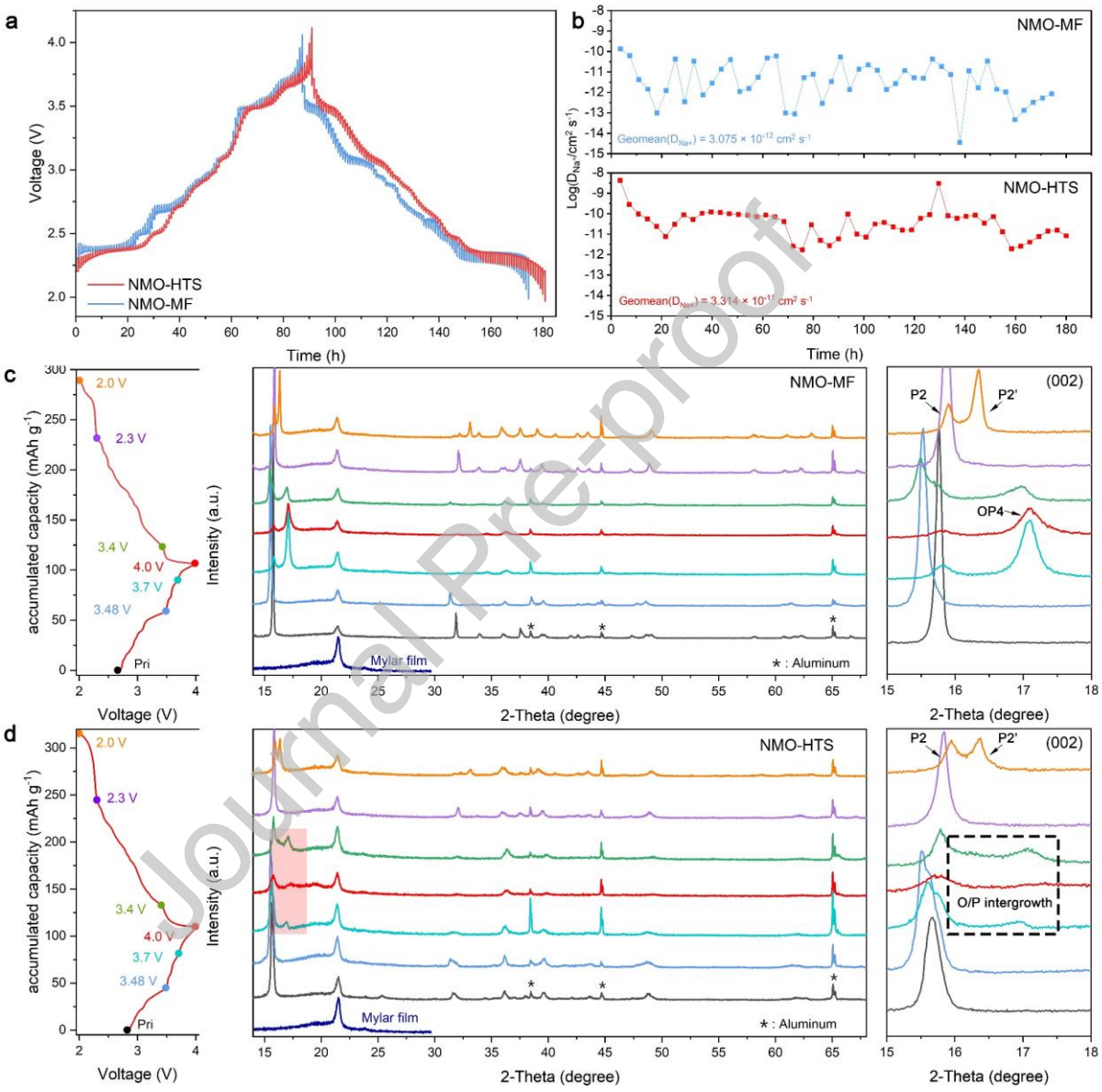

Fig. 4. Characterization of ionic motility and crystal structure evolution NMO materials. a) The GITT profiles and b) Na^+ diffusion coefficients (D_{Na+}) of NMO-MF and NMO-HTS electrodes. Ex situ XRD during the first charge-discharge cycle of c) NMO-MF and d) NMO-HTS. The cycling curves are shown on the left of each pattern and the magnified images of the (002) plane are shown on the right side of each pattern.

Generally, the NMO electrode undergoes multiple phase transitions in the high-voltage (P2-O2 phase transformation) and low-voltage (P2-P2’ phase transformation), which are linked to TM layer gliding and TM layer distortion, respectively [14,23]. The TM layer stacking faults in NMO-HTS are anticipated to exert a profound influence on the structural evolution of the material. A series of XRD spectra of NMO-MF and NMO-HTS cathodes during the first charge-discharge processes are depicted in **Fig. 4e-f**. Upon charging, NMO-MF initially undergoes a transition from the P2’ to P2 phases and then is accompanied by TM layer gliding to form the O-type stacking at high voltages. At 4.0 V, the material primarily exhibits the OP4 phase (intermediate phase between the P2 and O2 phases), with a small fraction of residual P2 phase. During discharge, a notable splitting of the $(002)_{P2}$ peak occurs as the voltage decreases to 2.0 V, indicating the formation of a P2’ phase structure (**Fig. 4e**). These structure evolutions are consistent with previous reports, and the repeated phase transitions in NMO-MF cathode inevitably lead to lattice defect accumulation and even structural collapse [23]. In contrast, NMO-HTS electrodes exhibit minor and continuous structural changes during cycling. Despite the diffraction peaks of NMO-HTS displaying weaker intensity than those of NMO-MF at pristine, they exhibit superior retention during the late stages of charging, while the (00*l*) and (10*l*) diffraction peaks of NMO-MF become almost unobserved. Compared to the significant emergence of the O-type stacking in NMO-MF, the NMO-HTS electrode manifests a broad peak at a higher diffraction degree besides the $(002)_{P2}$ peak during charging, indicative of a continuously varying O/P intergrowth structure [32,54]. Moreover, this O/P intergrowth structure maintains a broad peak and continuously reverts to the P2 phase structure during discharge. At the end of discharge, the P2' phase structure is also observed in the NMO-HTS

cathode; however, the proportion of the retained P2 phase in NMO-HTS is higher than that in NMO-MF, corresponding to minor structure distorted in NMO-HTS. In short, NMO-HTS exhibits a higher amount of Na^+ extraction/insertion, yet its structural changes are minor and continuous, which should stem from the hindering effect of the TM layer stacking faults on TM layer gliding and distortion. The higher structural reversibility of NMO-HTS also elucidates its superior cycling stability relative to NMO-MF in the LHCE electrolyte. (**Fig. 3g**).

3.5 Alleviative Mn Ion Vacancies by HTS

The different sintering processes could influence the formation of various ion vacancies within the materials. Firstly, XPS was employed to investigate the differences in oxygen vacancy (OV) content under different sintering conditions. The O *1s* spectra and fitting results of NMO-MF and NMO-HTS are shown in **Fig.** 5**a-b**. The peak at 529.6 eV corresponds to lattice oxygen bonded with TM ions (TM-O), while the peak at 531.7 eV is usually associated with OVs [55]. The XPS O *1s* spectra of NMO-MF and NMO-HTS samples exhibit similarity, with fitting results indicating a small proportion of OV signals in both samples, indicating the low content of OVs. Due to XPS providing chemical information mainly restricted to the surface of materials, EPR was further utilized to validate the OVs within the bulk of materials. As illustrated in **Fig. 5c**, the EPR signals centered at g = 2.003 confirm the presence of OVs in both samples. Consistent with the findings from XPS results, the OV content is minimal and comparable in the bulk of NMO-MF and NMO-HTS samples. On the other hand, the splitting energies observed in the Mn *3s* spectra (**Fig. 5d-e**) could indicate the average oxidation state of Mn ions. The splitting energies of NMO-MF and NMO-HTS are equal to 4.9 eV and 5.1 eV,

respectively, suggesting the lower average oxidation state of Mn ions in NMO-HTS than that of NMO-MF. Additionally, X-ray absorption near edge structure (XANES) analysis (**Fig. 5f**) reveals that the Mn K-edge position of NMO-HTS is lower than that of NMO-MF, further confirming the lower average oxidation state of Mn in the bulk phase of NMO-HTS. Given the similar OV content in NMO-MF and NMO-HTS, the difference in the average oxidation state of Mn ions should originate from the influence of Mn vacancies (MVs) within the TM layers. As the MV content decreases, the average oxidation state of Mn ions will decrease to maintain charge neutrality in the material. Conversely, an increase in MV content will raise the average oxidation state of Mn ions. The occupancy of Mn ions was determined through refined XRD results [20], as shown in **Fig. 5g** and **Table S2**, where the percentage of MVs in NMO-MF and NMO-HTS samples is ~3.1% and ~0.8%, respectively. The fewer MVs in NMO-HTS should be partly caused by the faster cooling rate of HTS technique than the quenching treatment [20,23], resulting in a lower Mn oxidation state compared to the NMO-MF.

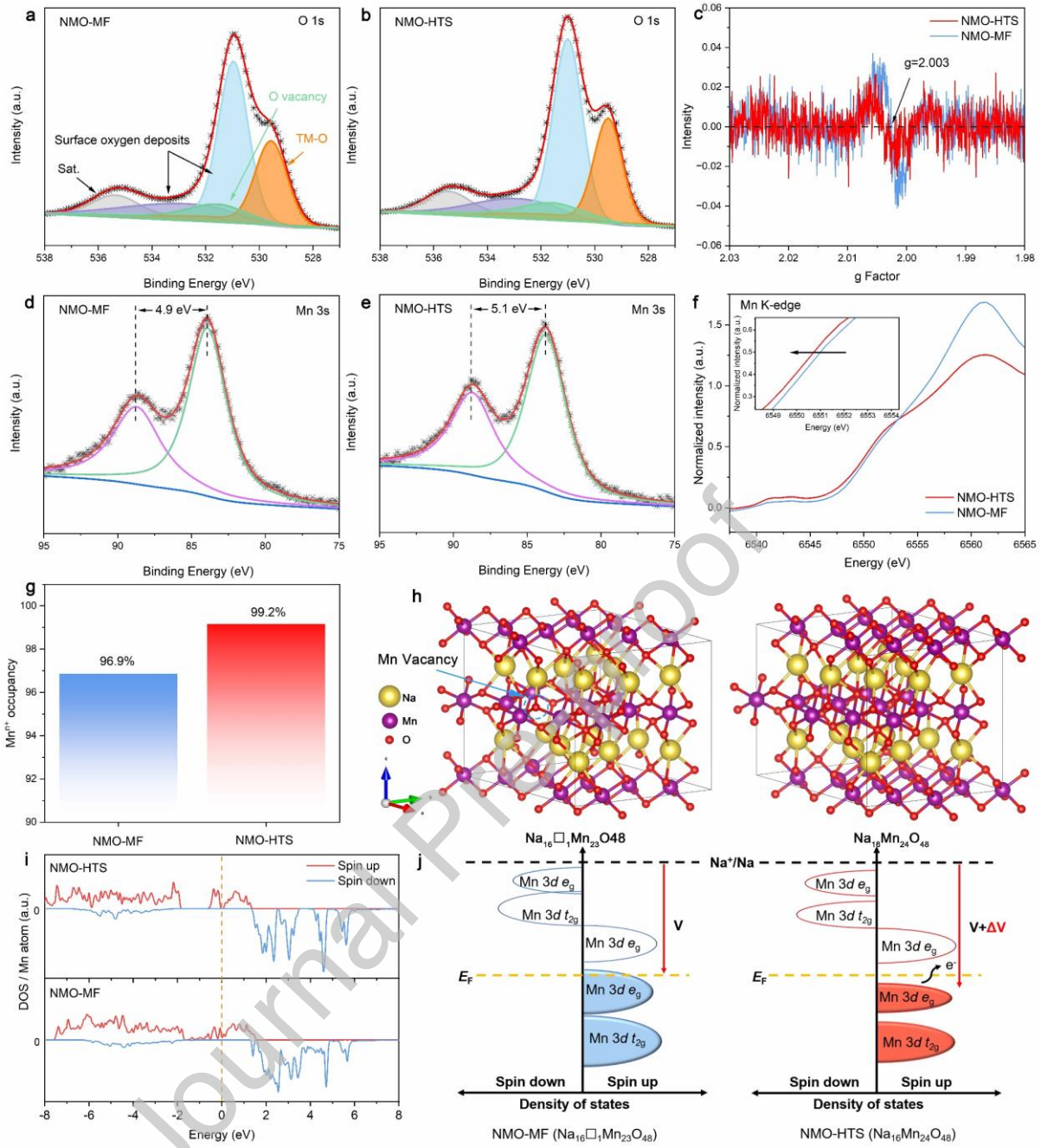

Fig. 5. Characterization and theoretical calculations of ion vacancies. XPS O*1s* spectra and fitting results for a) NMO-MF and b) NMO-HTS. c) EPR spectra of NMO-HTS and NMO-MF. XPS Mn*3s* spectra and fitting results for d) NMO-MF and e) NMO-HTS. f) Mn K-edge XANES spectra of NMO-MF and NMO-HTS. g) Mn ions occupancy obtained from XRD refinement. h) The lowest energy cation arrangements in the Na16□1Mn23O48 and Na16Mn24O48 supercells are obtained through theoretical calculations. i) PDOS analysis results for NMO-MF and NMO-HTS, and j) corresponding schematic band diagram.

Utilizing Density Functional Theory (DFT) calculations, we conducted an exploration of the influence of MVs within the TM layer on the electrochemical properties of the material. As

illustrated in **Fig. 5h**, the supercells of $Na_{16}\square_1Mn_{23}O_{48}$ ("□" representing MVs) and $Na_{16}Mn_{24}O_{48}$ were constructed respectively based on the MV content in NMO-MF and NMO-HTS to obtain their most stable crystal structures. The Mn redox potential is linked to the Mn *3d* electronic structure [55]. The Partial Density of States (PDOS) analysis results are presented in **Fig. 5i** and corresponding schematic band diagrams are delineated in **Fig. 5j**. In the case of NMO-MF containing MVs in the bulk phase, the Fermi level aligns with the spin-up Mn *3d* e_g electron-occupied states, indicating a propensity for electron transfer reactions within the bulk phase and lower redox potential (average discharge voltage of NMO-MF = 2.503 V). Conversely, for NMO-HTS nearly without MVs, the Mn *3d* e_g electron-occupied states reside below the Fermi level, rendering it less susceptible to electron transfer reactions and thereby exhibiting a higher redox potential (average discharge voltage of NMO-HTS = 2.652 V). To corroborate these findings, we implemented muffle furnace sintering followed by a slow cooling process to improve the MV concentration within the bulk phase of NMO material (*i.e.* NMO-MF-SC). The resulting MV proportion within the bulk phase of NMO-MF-SC approximated 11.9% (**Fig. S9** and **Table S3**), similar to previously reported values of ~13.3% [19]. Furthermore, as shown in **Fig. S10**, the Fermi level of NMO-MF-NC also aligns with its Mn *3d* e_g electron-occupied states, and its higher MV content leads to the much lower average discharge voltage of 2.452 V and capacity of 157 mAh g^{-1} (**Fig. S11**). Therefore, it could be concluded that a high concentration of MVs precipitates reduced operating voltages and capacities of NMO materials, thereby engendering diminished energy density. Conversely, the negligible MVs within the bulk phase of NMO-HTS confer upon it an improved energy density, consistent with the aforementioned electrochemical test results (**Fig. 2**).

3.6 Correlation Between Microstructure and Electrochemical Performance

To further investigate the correlation between the microstructure formed by HTS and its electrochemical performance, we varied the HTS sintering parameters, including cooling rate and sintering temperature. Firstly, we modified the HTS cooling process by introducing an isothermal cooling step to 550°C within 120 s before quenching. XRD results (**Fig. 6a**) reveal that the slow-cooled sample (NMO-HTS-SC) mainly adopts a P2 phase. Rietveld refinement results (**Fig. 6b** and **Table S4**) demonstrate that MV content in NMO-HTS-SC increased to 3.68%. As shown in **Fig. 6c**, the NMO-HTS-SC electrode exhibits a reduced capacity of 160 mAh g^{-1} and a lower average discharge voltage of 2.482 V. On the other hand, increasing the HTS sintering temperature to 1050°C (NMO-HTS-1050) and 1100°C (NMO-HTS-1100) revealed significant changes in stacking faults. Powder XRD patterns (**Fig. S12a**) confirm that the samples retained the P2' phase structure. However, ^{23}Na NMR spectra (**Fig. 6d**) show that the stacking fault signal at ~723 ppm diminished with rising sintering temperatures, disappearing entirely at 1100°C. This likely results from accelerated crystal growth and more ordered lattice arrangements at higher temperatures. It is worth noting that NMO-HTS-1050 and NMO-HTS-1100 electrodes display new small plateaus in their charge-discharge curves corresponding to Na^+-vacancy ordering during cycling. This phenomenon becomes more apparent as the degree of stacking faults decreases (**Fig. 6e-f**). The above results demonstrate that HTS sintering parameters significantly influence the microstructure of NMO materials, subsequently affecting their electrochemical performance. A faster cooling rate and lower sintering temperature help suppress Mn vacancies and promote stacking faults, respectively,

enabling NMO materials to achieve higher energy density while inhibiting the formation of Na^+-vacancy ordering formation.

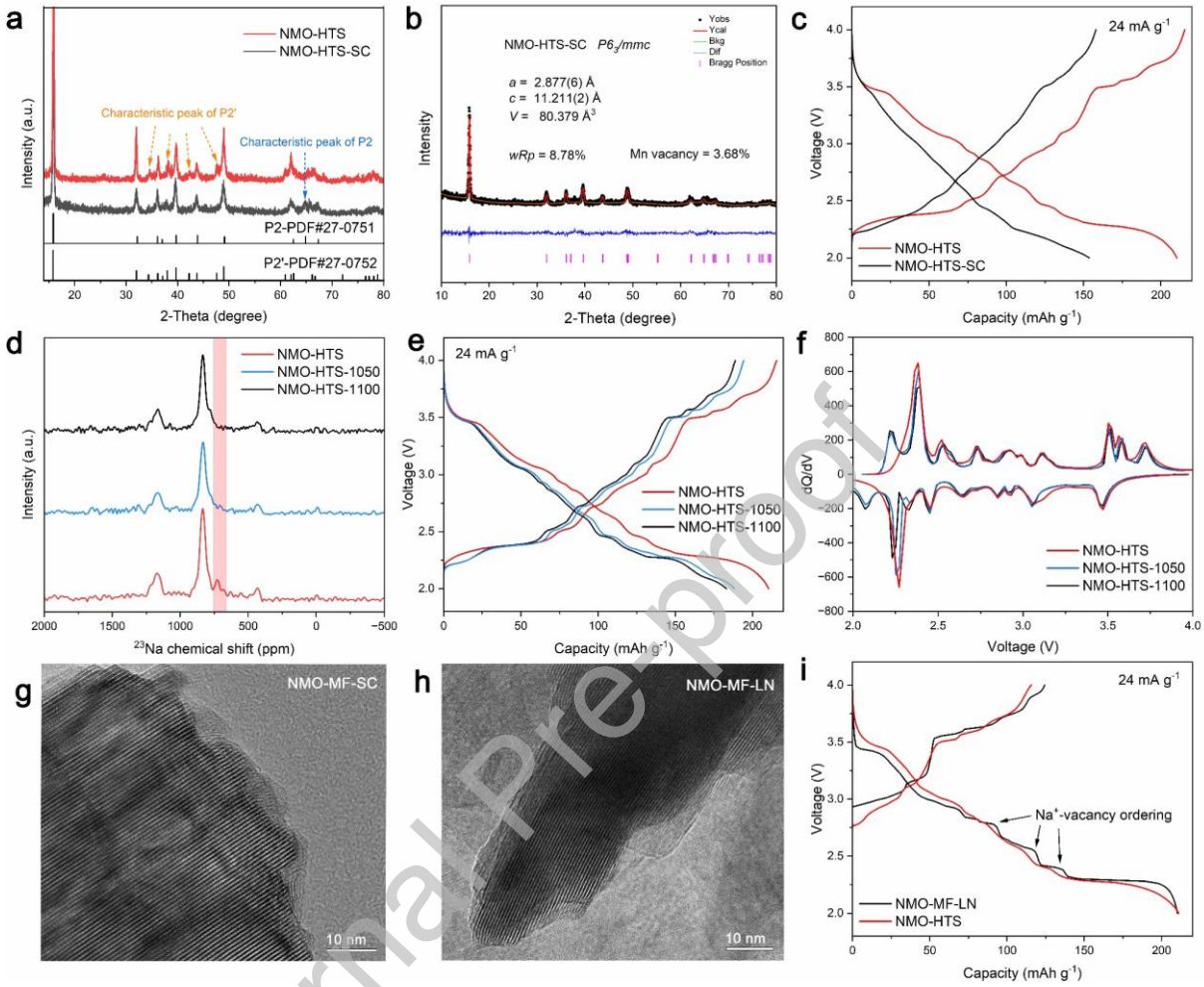

Fig. 6 a) Comparison of powder XRD patterns for NMO-HTS and NMO-HTS-SC. b) Rietveld refinement results of NMO-HTS-SC XRD data. c) Comparison of 2nd cycle charge-discharge curves for NMO-HTS and NMO-HTS-SC. d) ^{23}Na NMR spectra of NMO-HTS-1000, NMO-HTS-1050, and NMO-HTS-1100 samples. e) 2nd cycle charge-discharge curves and f) corresponding dQ/dV plots of NMO-HTS-1000, NMO-HTS-1050, and NMO-HTS-1100 electrodes. HRTEM images of g) NMO-MF-SC and h) NMO-MF-LN samples. i) Charge-discharge curves of NMO-MF-LN and NMO-HTS electrodes.

Another question is the potential correlation between MVs and stacking faults. To investigate this, we synthesized NMO-MF-LN by muffle furnace sintering followed by liquid nitrogen quenching. Unlike the slowly cooled NMO-MF-SC, NMO-MF-LN exhibited the typical P2' phase and a lower MV content of 0.13% (**Fig. S13** and **Table S5**), even less than

0.8% in NMO-HTS, reaffirming the strong dependence of MVs on cooling rate. HRTEM images (**Fig. 6g-h**) of NMO-MF-SC and NMO-MF-LN demonstrate that notable stacking faults are observed exclusively in the NMO-HTS sample despite differences in MV content, suggesting no obvious correlation between MVs and stacking faults. Thus, we believe that the formation of stacking faults should be mainly attributed to the ultrafast and non-equilibrium sintering conditions during HTS. Moreover, NMO-MF-LN and NMO-HTS (**Fig. 6i**) exhibit similar average discharge voltages of 2.62 V and 2.65 V, respectively. This aligns with the theoretical calculation results (**Fig. 5**), where similar MV contents in both materials lead to analogous Mn *3d* e_g orbital energy levels, resulting in similar average voltages. It also suggests that stacking faults have minimal influence on the Mn *3d* e_g orbitals and discharge voltage.

3.6 Universality and Expandability of HTS

Induced by the ultra-rapid heating and cooling rate conditions, HTS has been demonstrated to significantly influence the interlayer arrangement of TM layers and the content of intra-layer ion vacancies in NMO materials. Therefore, it is reasonable to assume that HTS is also a powerful tool for optimizing the crystal structures of other sodium-ion layered oxide materials when compared to conventional sintering methods. To demonstrate the universality of HTS, we sintered another three materials using the same method including the $Na_{0.67}Li_{0.05}Mg_{0.05}Al_{0.05}Ti_{0.05}Mn_{0.8}O_2$ (TM5), nickel-based $Na_{0.67}Ni_{0.25}Mn_{0.75}O_2$ (NNMO) and iron-based $Na_{0.67}Fe_{0.5}Mn_{0.5}O_2$ (NFMO) materials (labeled as TM5-HTS, NNMO-HTS and NFMO-HTS, respectively). These materials all exhibit higher capacity and voltage than the muffle furnace sintered counterparts (as displayed in **Fig. 7b-c** and **Fig. S14-S19**). Notably, in

these materials, TM5 contains four hetervalent ions doped (Li^+, Mg^{2+}, Al^{3+}, and Ti^{4+}), and the material synthesized by the muffle furnace contains observable $LiTi_2O_4$ and $NaMnTiO_4$ impurity peaks in the XRD spectrum (**Fig. 7a).** In striking contrast, HTS successfully ensures the introduction of four heterovalent metal ions into the TM5 material with a pure P2 phase structure and evenly distributed elements as indicated by XRD and SEM results (**Fig. S14**), which also demonstrates the significant advantage of HTS in improving phase purity induced by non-equilibrium reactions and fast reaction kinetics. Additionally, it is interesting to note that even if the muffle furnace sintered materials (NMO-MF, TM5-MF, NNMO-MF, NFMO-MF) or store aging materials (labeled as a hydrated phase structure H-NMO) are subjected to only 10 s HTS, the re-optimization of the material structure can be achieved. The treated materials (NMO-MF-HTS, TM5-MF-HTS, NNMO-MF-HTS, NFMO-MF-HTS) showed higher capacities and voltages than muffle furnace sintered counterparts (**Fig. 7b-c**). However, they are still lower than those of direct high-temperature shock synthesized samples (NMO-HTS, TM5-HTS, NNMO-HTS, NFMO-HTS). For the store aging materials (H-NMO), the sodium salt crystals (*e.g.* Na_2CO_3, $NaHCO_3$, *etc*.) on the surface of the H-NMO material were removed and the surface of H-NMO-HTS particles became smooth after HTS (**Fig. 7d-f**). The HTS treatment effectively restores degraded materials (**Fig. S20**), as evidenced by the higher initial capacity of the H-NMO-HTS electrode (187 mAh g^{-1}) compared to H-NMO and pristine NMO-MF sample while maintaining comparable cycling stability as illustrated in **Fig. 7h-i**. Therefore, these results strongly indicate that HTS technique not only enables the rapid synthesis of various sodium-ion layered oxide materials but also serves as an effective strategy

for material structural optimization and recovery, thereby enhancing the capacity and average discharge voltage of cathode materials.

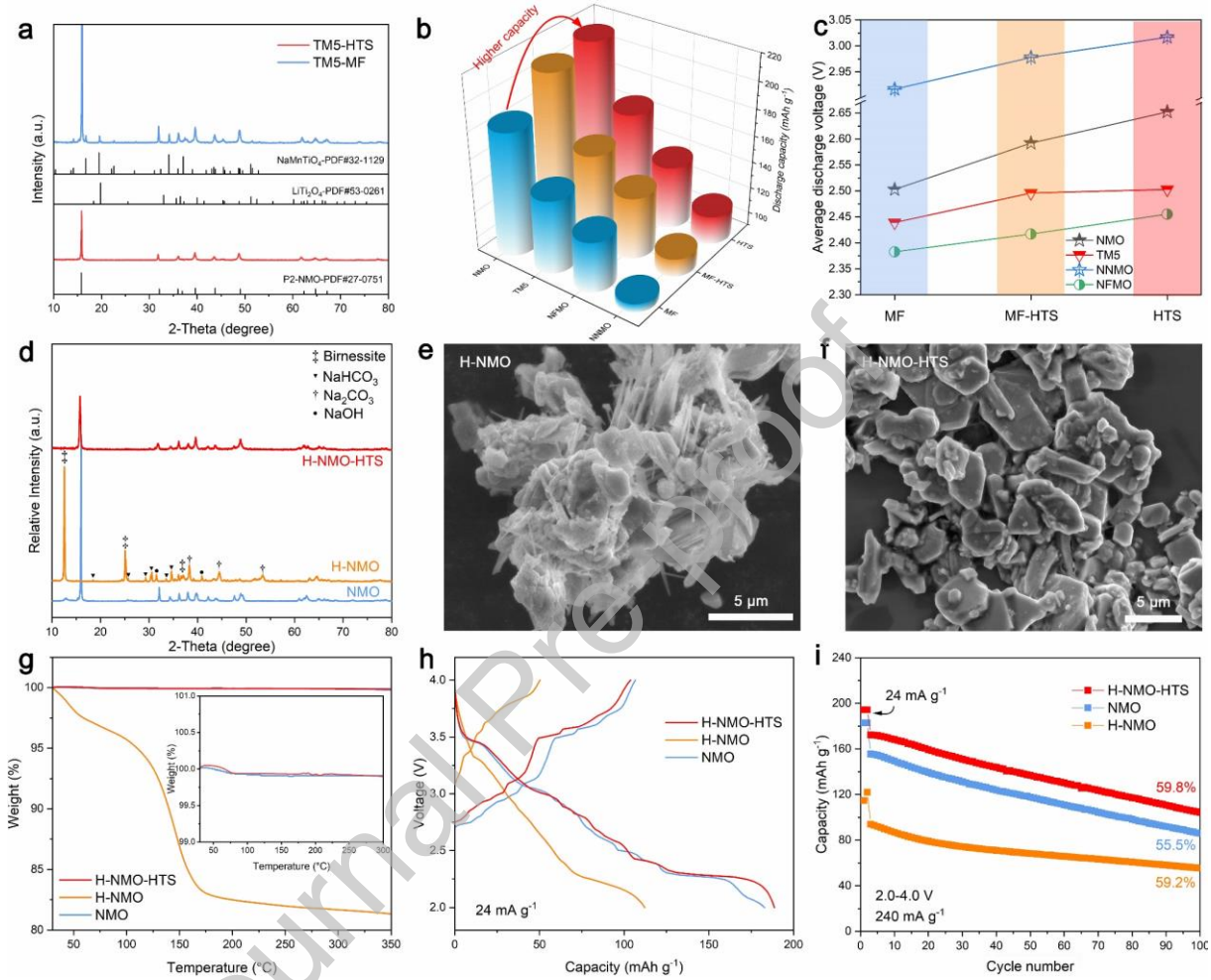

Fig. 7. Universality and Expandability of HTS strategy for sodium-ion layered oxides. a) Ex-situ XRD patterns of TM5-MF and TM5-HTS samples. Comparisons of b) discharge specific capacity and c) average voltage among Mn-based, Ni-based, and Fe-based sodium-ion layered oxide cathodes synthesized via muffle furnace sintering (MF), muffle furnace sintering followed by HTS treatment (MF-HTS), and one-step HTS. d) XRD patterns of NMO, H-NMO, and H-NMO-HTS powder materials. e) SEM images of H-NMO and f) H-NMO-HTS materials. g) Thermogravimetric curves of NMO, H-NMO, and H-NMO-HTS materials. h) The 1st cycle charge-discharge curves and i) cycling performance at 240 mA g^{-1} of NMO, H-NMO, and H-NMO-HTS electrodes.

4. Conclusion

In summary, this study elucidates the general applicability of the HTS technique for the rapid synthesis, material modification, and hydration recovery of sodium ion layered oxide cathodes, complemented by a comprehensive investigation of their structure-property relationships through multiple characterization techniques and electrochemical experiments. Taking NMO as a model material, we systematically explore the synthesis conditions enabled by HTS, achieving the ultrafast synthesis of NMO. HRTEM, EXAFS, and SS NMR reveal a typical TM layer stacking faults in NMO-HTS. GITT and XRD further corroborated the capability of the TM layer stacking faults to mitigate the Na^+-vacancies ordering and structural transformations during cycling, thereby enhancing the Na^+ mobility and structural stability of the material. On the other hand, XPS, XANES, and XRD refinement results confirm the negligible presence of MVs in NMO-HTS, which increases the redox-active centers, enabling high practical capacity. Furthermore, DFT calculation reveals that the elimination of MV leads to a lower Mn *3d* e_g orbital energy level, facilitating an improved Mn redox potential. As a result, the prepared NMO-HTS cathode exhibits superior electrochemical properties compared to NMO-MF synthesized by conventional solid-state method, delivering high energy density (559 Wh kg^{-1}), outstanding rate capability (108 mAh g^{-1} at 10C), and stable cycling performance in LHCE (93.7% capacity retention after 300 cycles). This study highlights the pivotal role of synthesis methods in modulating the structure and properties of sodium-ion layered oxides, paving the way for the development of cost-effective and high-performance cathodes for advanced SIBs.

Conflict of Interest

The authors declare no conflict of interest

Supplementary materials

Supplementary material associated with this article can be found, in the online version, at…

CRediT authorship contribution statement

Bizhu Zheng: Conceptualization, Investigation, Methodology, Data curation, Writing – original draft, Writing – review & editing. Hui Qian: Investigation, Methodology, Data curation, Writing – review & editing. Gangya Cheng: Investigation, Data curation, Writing – review & editing. Chen Yuan: Theoretical calculation, Software, Methodology. Yong Cheng: Investigation, TEM characterization, Data curation. Ming-Sheng Wang: Formal analysis, Writing – review & editing. Xiangsi Liu: Conceptualization, Funding acquisition, Investigation,Methodology, Data curation, Writing – original draft, Writing – review & editing. Yuxuan Xiang: Conceptualization, Supervision, Project administration, Funding acquisition, Writing – review & editing.

Acknowledgements

This work was supported by Research Center for Industries of the Future (RCIF) at Westlake University and Westlake Education Foundation, National Natural Science Foundation of China (grant nos 22309148) and Postdoctoral Science Foundation of China (grant nos 2023M733176). The author expresses gratitude to Dr. Xingyu Lu and Danyu Gu from Instrumentation and Service Center for Molecular Sciences at Westlake University for their support in SS NMR

measurements. The author thanks Xin Li from Instrumentation and Service Center for Molecular Sciences for the assistance with the thermal gravimetric analyzer measurement. The author also thanks Ying Nie from Instrumentation and Service Center for Physical Sciences at Westlake University for the help with the laser diffraction particle size analyzer measurement. The calculations were performed at Westlake High-Performance Computing Center.

References

[1] W. Zuo, A. Innocenti, M. Zarrabeitia, D. Bresser, Y. Yang, S. Passerini, Layered Oxide Cathodes for Sodium-Ion Batteries: Storage Mechanism, Electrochemistry, and Techno-economics, Acc Chem Res 56 (2023) 284-296. https://doi.org/10.1021/acs.accounts.2c00690.
[2] S. Chu, S. Guo, H. Zhou, Advanced cobalt-free cathode materials for sodium-ion batteries, Chem Soc Rev 50 (2021) 13189-13235. https://doi.org/10.1039/d1cs00442e.
[3] X. Sun, M. Ouyang, H. Hao, Surging lithium price will not impede the electric vehicle boom, Joule 6 (2022) 1738-1742. https://doi.org/10.1016/j.joule.2022.06.028.
[4] K. Chayambuka, G. Mulder, D.L. Danilov, P.H.L. Notten, From Li‐Ion Batteries toward Na‐Ion Chemistries: Challenges and Opportunities, Advanced Energy Materials 10 (2020) https://doi.org/10.1002/aenm.202001310.
[5] P.K. Nayak, L.T. Yang, W. Brehm, P. Adelhelm, From Lithium-Ion to Sodium-Ion Batteries: Advantages, Challenges, and Surprises, Angew Chem Int Edit 57 (2018) 102-120. https://doi.org/10.1002/anie.201703772.
[6] G.L. Xu, R. Amine, A. Abouimrane, H.Y. Che, M. Dahbi, Z.F. Ma, I. Saadoune, J. Alami, W.L. Mattis, F. Pan, Z.H. Chen, K. Amine, Challenges in Developing Electrodes, Electrolytes, and Diagnostics Tools to Understand and Advance Sodium-Ion Batteries, Advanced Energy Materials 8 (2018) 1702403-n/a. https://doi.org/ARTN 1702403 10.1002/aenm.201702403.
[7] N. Yabuuchi, K. Kubota, M. Dahbi, S. Komaba, Research Development on Sodium-Ion Batteries, Chemical Reviews 114 (2014) 11636-11682. https://doi.org/10.1021/cr500192f.
[8] W. Zuo, J. Qiu, X. Liu, B. Zheng, Y. Zhao, J. Li, H. He, K. Zhou, Z. Xiao, Q. Li, G.F. Ortiz, Y. Yang, Highly-stable P2–Na0.67MnO2 electrode enabled by lattice tailoring and surface engineering, Energy Storage Materials 26 (2020) 503-512. https://doi.org/10.1016/j.ensm.2019.11.024.
[9] C.L. Zhao, Q.D. Wang, Z.P. Yao, J.L. Wang, B. Sánchez-Lengeling, F.X. Ding, X.G. Qi, Y.X. Lu, X.D. Bai, B.H. Li, H. Li, A. Aspuru-Guzik, X.J. Huang, C. Delmas, M. Wagemaker, L.Q. Chen, Y.S. Hu, Rational design of layered oxide materials for sodium-ion batteries, Science 370 (2020) 708-+. https://doi.org/10.1126/science.aay9972.

[10] C.L. Zhao, Z.P. Yao, Q.D. Wang, H.F. Li, J.L. Wang, M. Liu, S. Ganapathy, Y.X. Lu, J. Cabana, B.H. Li, X.D. Bai, A. Aspuru-Guzik, M. Wagemaker, L.Q. Chen, Y.S. Hu, Revealing High Na-Content P2-Type Layered Oxides as Advanced Sodium-Ion Cathodes, Journal of the American Chemical Society 142 (2020) 5742-5750. https://doi.org/10.1021/jacs.9b13572.
[11] J.J. Liang, L.Y. Liu, X.S. Liu, X.C. Meng, L.Y. Zeng, J. Liu, J. Li, Z.C. Shi, Y. Yang, O3-Type NaCrO as a Superior Cathode Material for Sodium/Potassium-Ion Batteries Ensured by High Structural Reversibility, Acs Applied Materials & Interfaces 13 (2021) 22635-22645. https://doi.org/10.1021/acsami.1c04997.
[12] M. Lin, X.S. Liu, Y.X. Xiang, F. Wang, Y.P. Liu, R.Q. Fu, J. Cheng, Y. Yang, Unravelling the Fast Alkali-Ion Dynamics in Paramagnetic Battery Materials Combined with NMR and Deep-Potential Molecular Dynamics Simulation, Angew Chem Int Edit 60 (2021) 12547-12553. https://doi.org/10.1002/anie.202102740.
[13] F.X. Ding, C.L. Zhao, D.D. Xiao, X.H. Rong, H.B. Wang, Y.Q. Li, Y. Yang, Y.X. Lu, Y.S. Hu, Using High-Entropy Configuration Strategy to Design Na-Ion Layered Oxide Cathodes with Superior Electrochemical Performance and Thermal Stability, Journal of the American Chemical Society 144 (2022) 8286-8295. https://doi.org/10.1021/jacs.2c02353.
[14] Y. Sun, S.H. Guo, H.S. Zhou, Adverse effects of interlayer-gliding in layered transition-metal oxides on electrochemical sodium-ion storage, Energy & Environmental Science 12 (2019) 825-840. https://doi.org/10.1039/c8ee01006d.
[15] Z. Guo, H. Jiang, X. Sun, X. Li, Z. Liu, J. Zhang, J. Luo, J. Zhang, X.S. Tao, J. Ding, X. Han, R. Liu, Y. Chen, W. Hu, Ultrafast Non‐Equilibrium Phase Transition Induced Twin Boundaries of Spinel Lithium Manganate, Advanced Energy Materials 14 (2023) https://doi.org/10.1002/aenm.202302484.
[16] H. Huang, L. Zhang, H. Tian, J. Yan, J. Tong, X. Liu, H. Zhang, H. Huang, S.m. Hao, J. Gao, L. Yu, H. Li, J. Qiu, W. Zhou, Pulse High Temperature Sintering to Prepare Single‐Crystal High Nickel Oxide Cathodes with Enhanced Electrochemical Performance, Advanced Energy Materials 13 (2022) https://doi.org/10.1002/aenm.202203188.
[17] Z. Song, Y. Liu, Z. Guo, Z. Liu, Z. Li, J. Zhou, W. Liu, R. Liu, J. Zhang, J. Luo, H. Jiang, J. Ding, W. Hu, Y. Chen, Ultrafast Synthesis of Large‐Sized and Conductive Na3V2(PO4)2F3 Simultaneously Approaches High Tap Density, Rate and Cycling Capability, Advanced Functional Materials (2024) https://doi.org/10.1002/adfm.202313998.
[18] J.M. Paulsena, J.R. Dahn, Studies of the layered manganese bronzes, Na2/3[Mn1−xMx]O2 with M=Co, Ni, Li, and Li2/3[Mn1−xMx]O2 prepared by ion-exchange, Solid State Ionics 126 (1999) 3-24.
[19] R. Stoyanova, D. Carlier, M. Sendova-Vassileva, M. Yoncheva, E. Zhecheva, D. Nihtianova, C. Delmas, Stabilization of over-stoichiometric Mn4+ in layered Na2/3MnO2, Journal of Solid State Chemistry 183 (2010) 1372-1379. https://doi.org/10.1016/j.jssc.2010.04.024.
[20] X. Liu, G. Zhong, Z. Xiao, B. Zheng, W. Zuo, K. Zhou, H. Liu, Z. Liang, Y. Xiang, Z. Chen, G.F. Ortiz, R. Fu, Y. Yang, Al and Fe-containing Mn-based layered cathode with controlled vacancies for high-rate sodium ion batteries, Nano Energy 76 (2020) 104997. https://doi.org/10.1016/j.nanoen.2020.104997.

[21] C.L. Zhao, Q.D. Wang, Y.X. Lu, L.W. Jiang, L.L. Liu, X.Q. Yu, L.Q. Chen, B.H. Li, Y.S. Hu, Decreasing transition metal triggered oxygen redox activity in Na-deficient oxides, Energy Storage Materials 20 (2019) 395-400. https://doi.org/10.1016/j.ensm.2018.10.025.
[22] L. Yang, Z. Liu, S. Liu, M. Han, Q. Zhang, L. Gu, Q. Li, Z. Hu, X. Wang, H.-J. Lin, C.-T. Chen, J.-M. Chen, S.-C. Haw, Z. Wang, L. Chen, Superiority of native vacancies in activating anionic redox in P2-type Na2/3[Mn7/9Mg1/9 □ 1/9]O2, Nano Energy 78 (2020) https://doi.org/10.1016/j.nanoen.2020.105172.
[23] Y.T. Shinichi Kumakura, KeiKubota, Kuniko Chihara, and Shinichi Komaba, Sodium and Manganese Stoichiometry of P2‐Type Na2/3MnO2, Angew Chem Int Edit 55 (2016) 12760-12763. https://doi.org/10.1002/anie.201606415
10.1002/ange.201606415.
[24] Z.M. Xiao, W.H. Zuo, X.S. Liu, J.S. Xie, H.J. He, Y.X. Xiang, H.D. Liu, Y. Yang, Insights of the Electrochemical Reversibility of P2-Type Sodium Manganese Oxide Cathodes via Modulation of Transition Metal Vacancies, Acs Applied Materials & Interfaces 13 (2021) 38305-38314. https://doi.org/10.1021/acsami.1c09544.
[25] Y.J. Guo, R.X. Jin, M. Fan, W.P. Wang, S. Xin, L.J. Wan, Y.G. Guo, Sodium layered oxide cathodes: properties, practicality and prospects, Chem Soc Rev (2024) https://doi.org/10.1039/d4cs00415a.
[26] X. Li, X. Ma, D. Su, L. Liu, R. Chisnell, S.P. Ong, H. Chen, A. Toumar, J.-C. Idrobo, Y. Lei, J. Bai, F. Wang, J.W. Lynn, Y.S. Lee, G. Ceder, Direct visualization of the Jahn–Teller effect coupled to Na ordering in Na5/8MnO2, Nature Materials 13 (2014) 586-592. https://doi.org/10.1038/nmat3964.
[27] W.H. Zuo, X.S. Liu, J.M. Qiu, D.X. Zhang, Z.M. Xiao, J.S. Xie, F.C. Ren, J.M. Wang, Y.X. Li, G.F. Ortiz, W. Wen, S.Q. Wu, M.S. Wang, R.Q. Fu, Y. Yang, Engineering Na-layer spacings to stabilize Mn-based layered cathodes for sodium-ion batteries, Nature Communications 12 (2021) 4903. https://doi.org/ARTN 4903
10.1038/s41467-021-25074-9.
[28] X. Liu, W. Zuo, B. Zheng, Y. Xiang, K. Zhou, Z. Xiao, P. Shan, J. Shi, Q. Li, G. Zhong, R. Fu, Y. Yang, P2-Na0.67AlxMn1-xO2 : Cost-Effective, Stable and High-Rate Sodium Electrodes by Suppressing Phase Transitions and Enhancing Sodium Cation Mobility, Angewandte Chemie 58 (2019) 18086-18095. https://doi.org/10.1002/anie.201911698.
[29] P.-F. Wang, H.-R. Yao, X.-Y. Liu, Y.-X. Yin, J.-N. Zhang, Y. Wen, X. Yu, L. Gu, Y.-G. Guo, Na+/vacancy disordering promises high-rate Na-ion batteries, Science advances 4 (2018) eaar6018.
[30] X. Liu, C. Yuan, X. Zheng, G. Cheng, H. Qian, B. Zheng, X. Lu, Y. Yang, Y. Zhu, Y. Xiang, Stabilizing Interlayer Repulsion in Layered Sodium‐Ion Oxide Cathodes via Hierarchical Layer Modification, Advanced Materials (2024) https://doi.org/10.1002/adma.202407519.
[31] Y. Tang, Q. Zhang, W. Zuo, S. Zhou, G. Zeng, B. Zhang, H. Zhang, Z. Huang, L. Zheng, J. Xu, W. Yin, Y. Qiu, Y. Xiao, Q. Zhang, T. Zhao, H.-G. Liao, I. Hwang, C.-J. Sun, K. Amine, Q. Wang, Y. Sun, G.-L. Xu, L. Gu, Y. Qiao, S.-G. Sun, Sustainable layered cathode with suppressed phase transition for long-life sodium-ion batteries, Nature Sustainability 7 (2024) 348-359. https://doi.org/10.1038/s41893-024-01288-9.

[32] X. Wang, Q. Zhang, C. Zhao, H. Li, B. Zhang, G. Zeng, Y. Tang, Z. Huang, I. Hwang, H. Zhang, S. Zhou, Y. Qiu, Y. Xiao, J. Cabana, C.-J. Sun, K. Amine, Y. Sun, Q. Wang, G.-L. Xu, L. Gu, Y. Qiao, S.-G. Sun, Achieving a high-performance sodium-ion pouch cell by regulating intergrowth structures in a layered oxide cathode with anionic redox, Nature Energy 9 (2024) 184-196. https://doi.org/10.1038/s41560-023-01425-2.
[33] S. Kumakura, Y. Tahara, S. Sato, K. Kubota, S. Komaba, P′ 2-Na2/3Mn0.9Me0.1O2 (Me = Mg, Ti, Co, Ni, Cu, and Zn): Correlation between Orthorhombic Distortion and Electrochemical Property, Chemistry of Materials 29 (2017) 8958-8962. https://doi.org/10.1021/acs.chemmater.7b02772.
[34] A. Nie, L.Y. Gan, Y. Cheng, Q. Li, Y. Yuan, F. Mashayek, H. Wang, R. Klie, U. Schwingenschlogl, R. Shahbazian-Yassar, Twin boundary-assisted lithium ion transport, Nano Lett 15 (2015) 610-615. https://doi.org/10.1021/nl504087z.
[35] H. Chung, Y. Li, M. Zhang, A. Grenier, C. Mejia, D. Cheng, B. Sayahpour, C. Song, M.H. Shen, R. Huang, E.A. Wu, K.W. Chapman, S.J. Kim, Y.S. Meng, Mitigating Anisotropic Changes in Classical Layered Oxide Materials by Controlled Twin Boundary Defects for Long Cycle Life Li-Ion Batteries, Chemistry of Materials 34 (2022) 7302-7312. https://doi.org/10.1021/acs.chemmater.2c01234.
[36] Y. Yang, C. Gao, T. Luo, J. Song, T. Yang, H. Wang, K. Zhang, Y. Zuo, W. Xiao, Z. Jiang, T. Chen, D. Xia, Unlocking the Potential of Li-Rich Mn-Based Oxides for High-Rate Rechargeable Lithium-Ion Batteries, Adv Mater 35 (2023) e2307138. https://doi.org/10.1002/adma.202307138.
[37] C. Luan, L. Jiang, X. Zheng, Y. Cao, Z. Huang, Q. Lu, J. Li, Y. Wang, Y. Deng, A.L. Rogach, Direct observation of the ultrafast formation of cation-disordered rocksalt oxides as regenerable cathodes for lithium-ion batteries, Chemical Engineering Journal 462 (2023) https://doi.org/10.1016/j.cej.2023.142180.
[38] S. Dou, J. Xu, X. Cui, W. Liu, Z. Zhang, Y. Deng, W. Hu, Y. Chen, High‐Temperature Shock Enabled Nanomanufacturing for Energy‐Related Applications, Advanced Energy Materials 10 (2020) https://doi.org/10.1002/aenm.202001331.
[39] M.Z. Chen, Q.N. Liu, S.W. Wang, E.H. Wang, X.D. Guo, S.L. Chou, High-Abundance and Low-Cost Metal-Based Cathode Materials for Sodium-Ion Batteries: Problems, Progress, and Key Technologies, Advanced Energy Materials 9 (2019) https://doi.org/ARTN 1803609 10.1002/aenm.201803609.
[40] W. Zhu, J. Zhang, J. Luo, C. Zeng, H. Su, J. Zhang, R. Liu, E. Hu, Y. Liu, W.D. Liu, Y. Chen, W. Hu, Y. Xu, Ultrafast Non‐Equilibrium Synthesis of Cathode Materials for Li‐Ion Batteries, Advanced Materials 35 (2022) https://doi.org/10.1002/adma.202208974.
[41] H. Jiang, C. Zeng, W. Zhu, J. Luo, Z. Liu, J. Zhang, R. Liu, Y. Xu, Y. Chen, W. Hu, Boosting cycling stability by regulating surface oxygen vacancies of LNMO by rapid calcination, Nano Research 17 (2023) 2671-2677. https://doi.org/10.1007/s12274-023-6076-1.
[42] Z. Liu, J. Zhang, J. Luo, Z. Guo, H. Jiang, Z. Li, Y. Liu, Z. Song, R. Liu, W.-D. Liu, W. Hu, Y. Chen, Approaching Ultimate Synthesis Reaction Rate of Ni-Rich Layered Cathodes for Lithium-Ion Batteries, Nano-Micro Letters 16 (2024) https://doi.org/10.1007/s40820-024-01436-y.
[43] J. Luo, J. Zhang, Z. Guo, Z. Liu, C. Wang, H. Jiang, J. Zhang, L. Fan, H. Zhu, Y. Xu, R. Liu, J. Ding, Y. Chen, W. Hu, Coupling Antisite Defect and Lattice Tensile Stimulates Facile

Isotropic Li‐Ion Diffusion, Advanced Materials (2024) https://doi.org/10.1002/adma.202405956.
[44] B.H. Toby, EXPGUI, a graphical user interface for GSAS, Journal of Applied Crystallography 34 (2001) 210-213. https://doi.org/Doi 10.1107/S0021889801002242.
[45] A.N.-E.S.M. Kozlov, F. Viñes, F. Illas, Electronic-structure-based chemical descriptors:(in) dependence on self-interaction and Hartree-Fock exchange, J Phys. Rev. B 54 (1996) 29.
[46] P.E. Blöchl, Projector augmented-wave method, J Physical review B 50 (1994) 17953.
[47] J.P. Perdew, K. Burke, M. Ernzerhof, Generalized gradient approximation made simple, J Physical review letters 77 (1996) 3865.
[48] R.J. Clément, J. Billaud, A.R. Armstrong, G. Singh, T. Rojo, P.G. Bruce, C.P. Grey, Structurally stable Mg-doped P2-Na2/3Mn1-yMgyO2 sodium-ion battery cathodes with high rate performance: insights from electrochemical, NMR and diffraction studies, Energy & Environmental Science 9 (2016) 3240-3251. https://doi.org/10.1039/c6ee01750a.
[49] Q. Zou, C. Xu, J. Zhang, D. Wang, H. Chen, G. Zhong, C. Lu, Z. Peng, Structure and Performance of NaxMn0.85Al0.1Fe0.05O2 (0.7 </= x </= 1.0) Composite Materials for Sodium-Ion Batteries, ACS Appl Mater Interfaces (2022) https://doi.org/10.1021/acsami.2c03115.
[50] M.A. Syed, M. Salehabadi, M.N. Obrovac, High Energy Density Large Particle LiFePO(4), Chem Mater 36 (2024) 803-814. https://doi.org/10.1021/acs.chemmater.3c02301.
[51] D. Tie, G.F. Gao, F. Xia, R.Y. Yue, Q.J. Wang, R.J. Qi, B. Wang, Y.F. Zhao, Modulating the Interlayer Spacing and Na/Vacancy Disordering of P2-Na0.67MnO2 for Fast Diffusion and High-Rate Sodium Storage, Acs Applied Materials & Interfaces 11 (2019) 6978-6985. https://doi.org/10.1021/acsami.8b19134.
[52] B. Xiao, Y. Zheng, M. Song, X. Liu, G.H. Lee, F. Omenya, X. Yang, M.H. Engelhard, D. Reed, W. Yang, K. Amine, G.L. Xu, P.B. Balbuena, X. Li, Protonation Stimulates the Layered to Rock Salt Phase Transition of Ni‐Rich Sodium Cathodes, Advanced Materials 36 (2024) https://doi.org/10.1002/adma.202308380.
[53] J. Zheng, S. Chen, W. Zhao, J. Song, M.H. Engelhard, J.-G. Zhang, Extremely Stable Sodium Metal Batteries Enabled by Localized High-Concentration Electrolytes, ACS Energy Letters 3 (2018) 315-321. https://doi.org/10.1021/acsenergylett.7b01213.
[54] J.W. Somerville, A. Sobkowiak, N. Tapia-Ruiz, J. Billaud, J.G. Lozano, R.A. House, L.C. Gallington, T. Ericsson, L. Häggström, M.R. Roberts, U. Maitra, P.G. Bruce, Nature of the "Z"-phase in layered Na-ion battery cathodes, Energy & Environmental Science 12 (2019) 2223-2232. https://doi.org/10.1039/c8ee02991a.
[55] J. Jin, Y. Liu, X. Zhao, H. Liu, S. Deng, Q. Shen, Y. Hou, H. Qi, X. Xing, L. Jiao, J. Chen, Annealing in Argon Universally Upgrades the Na-Storage Performance of Mn-Based Layered Oxide Cathodes by Creating Bulk Oxygen Vacancies, Angewandte Chemie (2023) e202219230. https://doi.org/10.1002/anie.202219230.

The ultrafast synthesis of P2-$Na_{0.67}MnO_2$ through the high-temperature shock technique is accomplished in ~70 s, resulting in a remarkable 21.5% enhancement in energy density, superior high-rate capability, and enhanced cost-effectiveness for sodium-ion batteries.

ToC figure

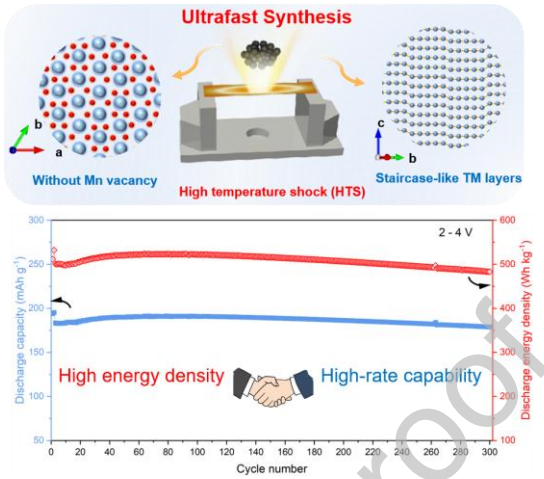

Declaration of interests

☒ The authors declare that they have no known competing financial interests or personal relationships that could have appeared to influence the work reported in this paper.

☐ The authors declare the following financial interests/personal relationships which may be considered as potential competing interests: